Low power optical phase shifter using liquid crystal actuation on a silicon photonics platform

LUKAS VAN ISEGHEM,[1,2] ● EWOUT PICAVET,[1,2,3,4] ALAIN YUJI TAKABAYASHI,[5] PIERRE EDINGER,[6] ● UMAR KHAN,[1,2] PETER VERHEYEN,[7] NIELS QUACK,[5] KRISTINN B. GYLFASON,[6] ● KLAARTJE DE BUYSSER,[3] JEROEN BEECKMAN,[2,4] ● AND WIM BOGAERTS[1,2,*] ●

[1] *Photonics Research Group, Ghent University - IMEC, Dept. of Information Technology, Belgium*
[2] *Center for Nano- and Biophotonics (NB Photonics), Ghent University, Belgium*
[3] *Sol-gel Centre for Research on Inorganic Powders and Thin films Synthesis, Ghent University, Dept. of Chemistry, Belgium*
[4] *Liquid Crystals and Photonics Group, Ghent University, Dept. of Electronics and Information Systems, Belgium*
[5] *École Polytechnique Fédérale de Lausanne, Switzerland*
[6] *KTH Royal Institute of Technology, Stockholm, Sweden*
[7] *IMEC vzw, 3DSIP department, Leuven, Belgium*
*wim.bogaerts@ugent.be

Abstract: Low-power and compact phase shifters are crucial for large photonic circuits, both to cope with variability and to create programmable waveguide circuits scaling to thousands of tuning elements. This work demonstrates a liquid crystal phase shifter where there is a lateral silicon electrode "rail" on one side of the waveguide core. Using this architecture, a strong quasi-static electric field $E_{\text{actuation}}$ can be applied over the gap, which is filled with liquid crystal cladding material, with modest voltages. Because the mode is largely confined in the waveguide, optical losses are limited, compared to earlier experiments with slot waveguides. The liquid crystal is deposited locally on three different device variations using inkjet printing. The local deposition avoids unwanted interference of the liquid crystal with other optical components such as grating couplers. Measurements show similar trends as simulations of the liquid crystal orientations. For one device with a length of 50 μm, a phase shift of almost 0.9π is shown at 10 V_{RMS}. We also discuss the challenges with this first demonstration of this phase shifter geometry using a silicon side-rail as an electrode.

1.   Introduction

Many applications in integrated photonic circuits require low-power and compact phase shifters, both to cope with variability during fabrication and operation and to create programmable waveguide circuits scaling to hundreds or thousands of tuning elements. In general, electro-optic phenomena that can be exploited to induce a phase shift exhibit a trade-off between actuation speed and magnitude of the effect. While high-speed effects are required for modulation, the slower but stronger effects are preferred for quasi-static tuning because they enable phase shifters with a short optical path length [1].

Like most silicon photonics technologies, IMEC's silicon photonics platform, iSiPP50G [2], provides a strong, low-speed tuning effect through heaters implemented using tungsten resistors, doped silicon resistors or PN junctions. While these heaters can be made compact, they are power hungry and susceptible to thermal crosstalk [3]. One method for creating compact, low-power phase shifters exploits mechanical actuation of a perturbation close to the waveguide, building on techniques from micro-electromechanical systems (MEMS). In [4] a comb-drive is used to

move a silicon rail closer/further from the waveguide core, changing the effective index of the propagating mode, which results in a strong phase shift. In this letter, we used the same device geometry to induce a phase shift with the help of a liquid crystal cladding.

Liquid crystals (LC) are highly anisotropic materials that have a quasi-crystalline arrangement, and where the director (i.e. the average orientation of the molecules) can be rotated by an external electric field. This makes the materials attractive to implement electro-optic phase shifters. While it is possible to implement waveguides directly into liquid crystals [5,6], it is easier to integrate it as a cladding material for silicon photonic waveguides [7–11].

Due to the evanescent field of the waveguide mode in the LC cladding, a change in LC orientation will lead to a modification of the mode's effective refractive index. One of the issues in these configurations demonstrated in earlier works is that the electrodes for applying voltage over the LC layer need to be far away from the optical mode to avoid optical absorption losses, and because of the large distance between the electrodes, high operating voltages up to 100 V are needed [7,9,11].

One way to mitigate these high voltages is applying the voltage across a narrow gap, increasing $E_{actuation}$. This can be accomplished using a a strip loaded slot waveguide infiltrated with LC, which has a narrow gap (slot) to realize strong actuation fields $E_{actuation}$ with low voltages when the silicon is used as an electrode [12]. The concentrated electric field of the optical mode in the slot has a large overlap with the rotation of the director (a vector describing the average direction of the molecules, indicated as $\vec{n}$ in Fig. 1) , leading to a strong electro-optic response. Even though the slot waveguide mode has a strong interaction with the director changes of the LC, this approach suffers from high optical losses because of the transitions between the slot waveguide and the regular waveguide, and increased scattering losses due to the concentrated electric field of the optical mode interacting with the sidewall roughness of the slot.
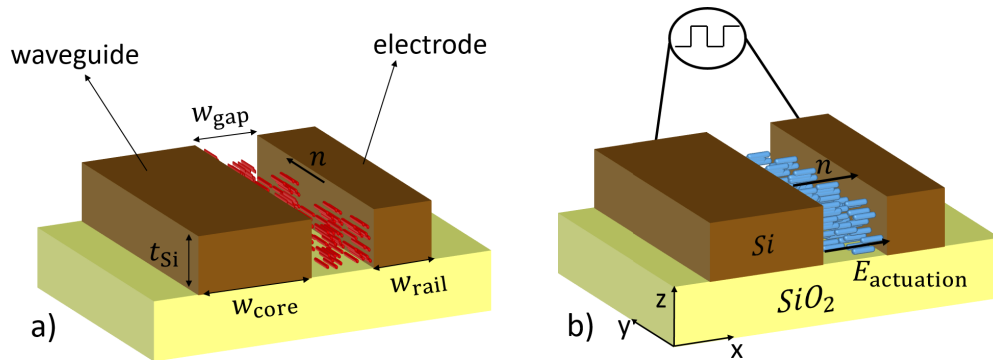

Fig. 1. Operation principle of the phase shifter. a) When no voltage is applied the LC director aligns itself with the longitudinal direction of the waveguide, indicated by the director $\vec{n}$. In this paper both the gap and waveguide width are varied to observe their effect on device performance. b) the reorientation when applying a square wave between the waveguide and electrode, where the director is aligned with the quasi-static electric field $E_{actuation}$.

This work tries to mitigate these loss contributions by keeping confinement in a regular single mode waveguide where the evanescent field of the propagating mode is influenced, rather then pushing the entire optical mode into a slot.

In this demonstration we used the phase shifter devices from [4], originally designed for MEMS-actuation, to implement an efficient liquid crystal (LC) phase shifter. It consists of a single mode waveguide that keeps the propagating mode mostly confined inside the core, and which is accompanied by a silicon side-rail operating as electrode on one side of the waveguide.

The waveguide core is grounded, so the voltage on the side-rail is applied directly over the gap leading to a strong actuation field $E_{\text{actuation}}$ at low voltages. Inside the gap, the evanescent tail of the TE mode of the small high-contrast waveguide core are quite large due to the sharp discontinuity of refractive index on the sidewall. As a result, a change of the material properties inside the gap still has a considerable effect on the effective index of the propagating mode. In addition, the silicon side-rail also acts as an index perturbation, pulling the optical mode a bit more into the gap, effective strengthening the electro-optic response.

The integration of the liquid crystal material with the silicon waveguides introduces its own challenges. In earlier work the LC was deposited over a larger region of the photonic chip, held in place by a glass plate [7,9,11]. This complicates the assembly, and also makes it difficult to combine the LC with other functions implemented with silicon photonics, such as modulators and detectors. In this work we use an inkjet printing technique in the fabrication of the devices where the LC is applied locally into recessed cavities on the chip where the waveguide is locally exposed. This avoids unwanted interference of the LC with other components (such as grating couplers) which remain encapsulated in an silicon dioxide dielectric cladding.

2.   Operational principle

2.1.   Side-rail as electrode

The optical phase shift can be induced by locally applying a voltage across the gap filled with liquid crystal, where the evanescent field of the waveguide mode will be affected by the reorientation of the liquid crystal. The operation principle of this device is shown in Fig. 1. A narrow silicon rail structure ($w_{\text{rail}} = 220\,\text{nm}$), which is optically in cut-off at the operational wavelength of 1550 nm, acts as an electrode to deliver a local voltage over the gap with the waveguide core, which is grounded. The thickness (height) of the silicon layer is equal for all simulated and measured devices, $t_{\text{Si}} = 220\ nm$. In this paper 3 different geometries are investigated with both simulation and measurements: ($w_{\text{core}} = 400\ nm$, $w_{\text{gap}} = 250\ nm$), ($w_{\text{core}} = 400\ nm$, $w_{\text{gap}} = 350\ nm$) and ($w_{\text{core}} = 450\ nm$, $w_{\text{gap}} = 250\ nm$).

When no voltage is applied, the boundary conditions of the surfaces cause the liquid crystal director in the gap to align itself parallel with the waveguide (as can be seen in Fig. 1(a))). [13] Because LC is an anisotropic material it exhibits an extra-ordinary index n_{e} parallel to the director $\vec{n}$ leading to optical birefringence, $\Delta n = n_{\text{e}} - n_{\text{o}}$. In this work we use commercially available LC mixture named E7 with the ordinary refractive index ($\lambda = 1.55\mu m$) $n_{\text{o}} \approx 1.5$, the optical birefringence $\Delta n \approx 0.2$, and the dielectric anisotropy ($f_{\text{actuation}} = 1kHz$) $\Delta\varepsilon = 11.1$ (the anisotropy for $\vec{E}_{\text{actuation}}$). [14–16]

When w_{gap} is sufficiently small (i.e. 250 nm), we can induce a strong quasi-static electric field $\vec{E}_{\text{actuation}}$ at voltages below 5 V. This is much lower than experiments with electrodes multiple μm away from the waveguide, which required voltages up to 100 V [7,9,11]. The local electric field causes the LC director to rotate, aligning itself with the applied field, which changes the optical permittivity tensor of the material. The electric field of a propagating TE mode has a strong interaction with this rotating director because the main electric field component, E_x, is in the plane of the director rotation, making this field component interact with n_{e} at 0 V and n_{o} at full reorientation in the gap.

The change in effective refractive index of this propagating mode results in a phase shift compared to the situation drawn in Fig. 1(a)).

$$\Delta\phi = \frac{2\Delta n_{\text{eff}} L_{\text{device}}}{\lambda_0} * \pi \tag{1}$$

A narrower gap increases the electric field between the waveguide and the side-rail, creating a stronger reorientation of the director closer to the waveguide edge at similar voltages. Close to

the surface the molecules "stick" to the surface (a phenomenon referred to as anchoring of the director, elaborated further in 2.3.1), leading to a director profile as illustrated on Fig. 2. This curve visualizes the variation of the twist of the director (angle ϕ as defined in Fig. 5) in the gap area indicated in red on Fig. 3 and shows how reorientation is weaker closer to the waveguide edge. One can notice the director profile function is a function of x/w_{gap}, making the director profile symmetric for any w_{gap} (ϕ_{max} will move closer to the waveguide edge when making the gap smaller). This implies that a narrower gap will increase director orientation close to the waveguide edge at the same actuation voltage, due to an increasing $\vec{E}_{\text{actuation}}$. In section 2.2 we discuss how the high refractive index of a silicon side-rail enhances the optical field E_{x} over the entire gap, not just close to the waveguide edge (besides the use as an electrode).
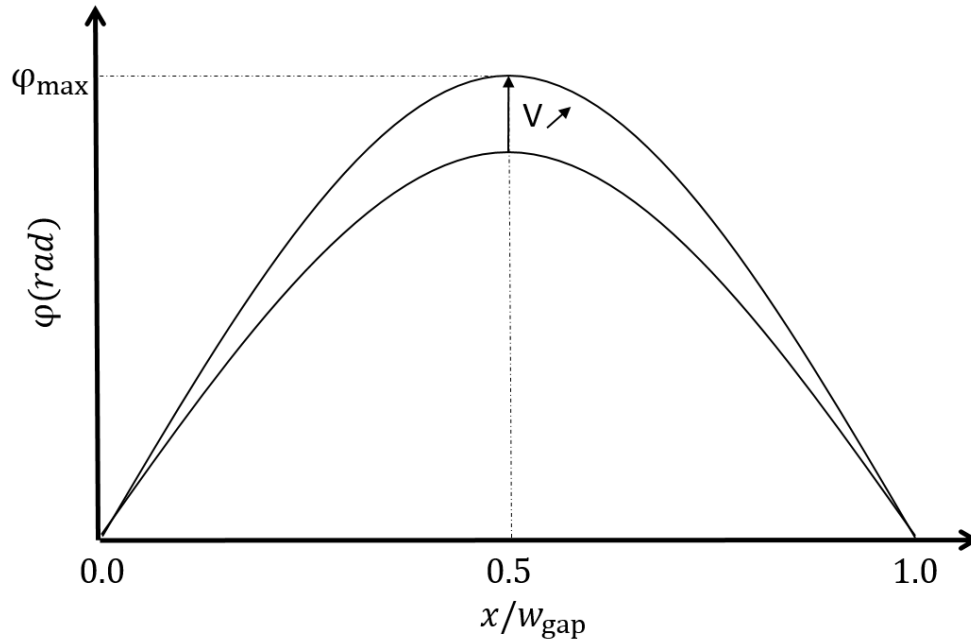

Fig. 2. Example distribution of the twist of the director in the gap. The molecules tend to "stick" to surfaces, making reorientation close to the surface smaller (as explained later). Because the evanescent tail of E_{x} in the gap has higher power closer to the waveguide core (as can be seen in Fig. 4), the change in director closer to the waveguide will produce a more significant Δn_{eff}. Since this curve is normalized to w_{gap}, narrowing the gap results on stronger director changes closer to the waveguide core.

2.2. *Side-rail as an index perturbation to increase optical confinement*

Usually one expects confinement in the waveguide core to increased when a high-index material is added to the cladding, but in this section we show this actually has the opposite effect when using this geometry. While the side-rail acting as an electrode creates strong quasi-static electric fields $\vec{E}_{\text{actuation}}$ to rotate the LC molecules, it also enhances this electro-optic effect as an index perturbation in the cladding. Intuitively, the high refractive index of the silicon side-rail pulls the optical waveguide somewhat more into the gap where it can interact with the liquid crystal.

As mentioned in section 2.1, a higher optical confinement of the waveguide mode in the gap between the core and the rail will increase the overlap with the actuated liquid crystal, improving the actuation efficiency of the phase shifter. This increased confinement is due to two effects: The silicon side rail adds additional high-index material next to the core, moving the 'center of
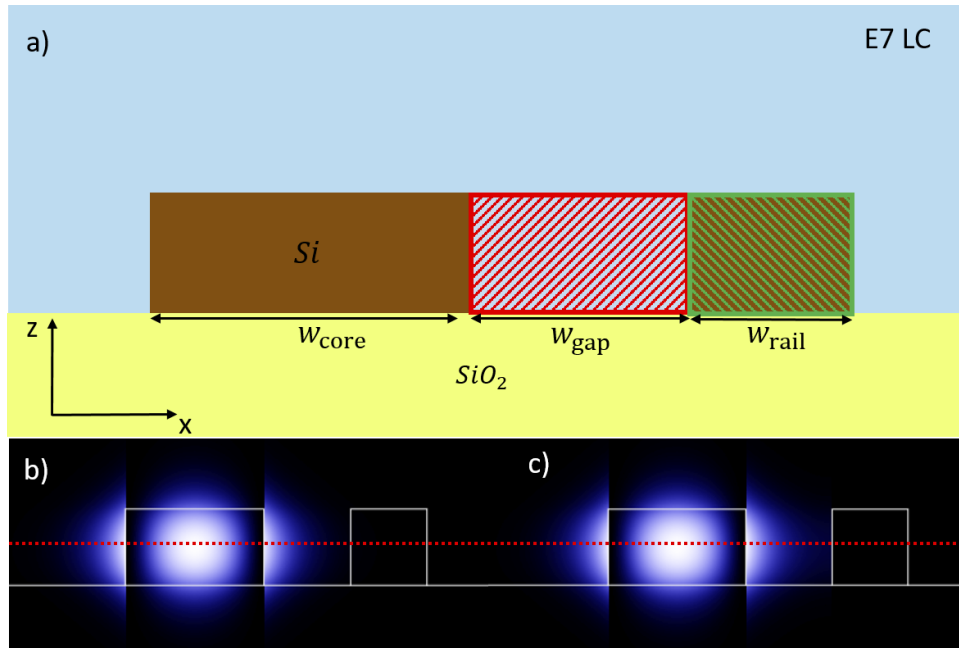
Fig. 3. a) 2D simulation window of geometry. Blue is the E7 LC cladding, simulations are carried out using both an E7 LC filled side-rail (matching the surrounding LC at $V = 0$ V_{RMS}) and a silicon side-rail. Color markings are used to address areas in text. b) Mode plot of $|E_x|^2$ for a side-rail filled with E7 LC as oriented in Fig. 1(a). c) Mode plot for a silicon side-rail ($n = 3.45$). The red dashed line indicate the position of the 1 dimensional field plots presented in Fig. 4

gravity' of the guided waveguide mode, bringing more light into the narrow gap. On top of that, the high refractive index contrast between the silicon core/rail and the liquid crystal induces a strong discontinuity of the E_x component of the optical field at the silicon/LC interfaces. Because there are now two such interfaces, the field in the narrow gap is enhanced, not just near the interfaces, but in the entire gap. This is similar to the field enhancement in a slot waveguide, but here we have kept a strong asymmetry to avoid very abrupt changes in the mode profile and make tapering to a regular waveguide easier.

To illustrate the enhancement effect of the high-index side-rail, we simulate a geometry where the area occupied by the side-rail is replaced with the same E7 LC oriented as in Fig. 1(a). We do keep the same electric fields on the liquid crystals as we would have in the case of a silicon side rail, so this is an entirely hypothetical configuration that allows us to separate the influence of increased director orientation on the phase shift from the index perturbation created using the silicon rail. However, it helps to illustrate that in the case of a side-rail which matches the refractive index of the surrounding LC (for $V = 0$ V_{RMS}), the actuation effect is weaker.

Figure 4 shows simulation results with and without actuation of the LC, meaning V = 5 V_{RMS} and V = 0V_{RMS}. When V = 0V_{RMS} and the LC cladding has a uniform orientation as shown in Fig. 1(a)) (this configuration is also shown in Fig. 5(a))). As mentioned before, we compare simulation results using an E7 LC filled side-rail with results with the silicon side-rail. The resulting E_x of the guided mode on the red dashed line shown in as in Fig. 3(b)) and c) is plotted in Fig. 4. The plots in Fig. 4 a), c) and e) show simulation results of the side-rail filled with E7 LC and the plots in Fig. 4 b), d) and f) show simulation results with a silicon side-rail. For each simulation result with $V = 0$ V_{RMS} the confinement factor of the waveguide core is calculated for

the three measured device geometries: $w_{core} = 400\,nm$ with $w_{gap} = 250\,nm$ labeled as *wg400g250* and plotted in graphs a) and b) on Fig. 4, $w_{core} = 450\,nm$ with $w_{gap} = 250\,nm$ labeled as *wg450g250* and plotted in graphs c) and d) on Fig. 4, $w_{core} = 400\,nm$ with $w_{gap} = 350\,nm$ labeled as *wg400g350* and plotted in graphs e) and f) on Fig. 4. We only consider the *x*-component of the electrical field strength in these calculations since this has the main contribution to the effective index of the TE mode, and the main component interacting with the director change in the gap.
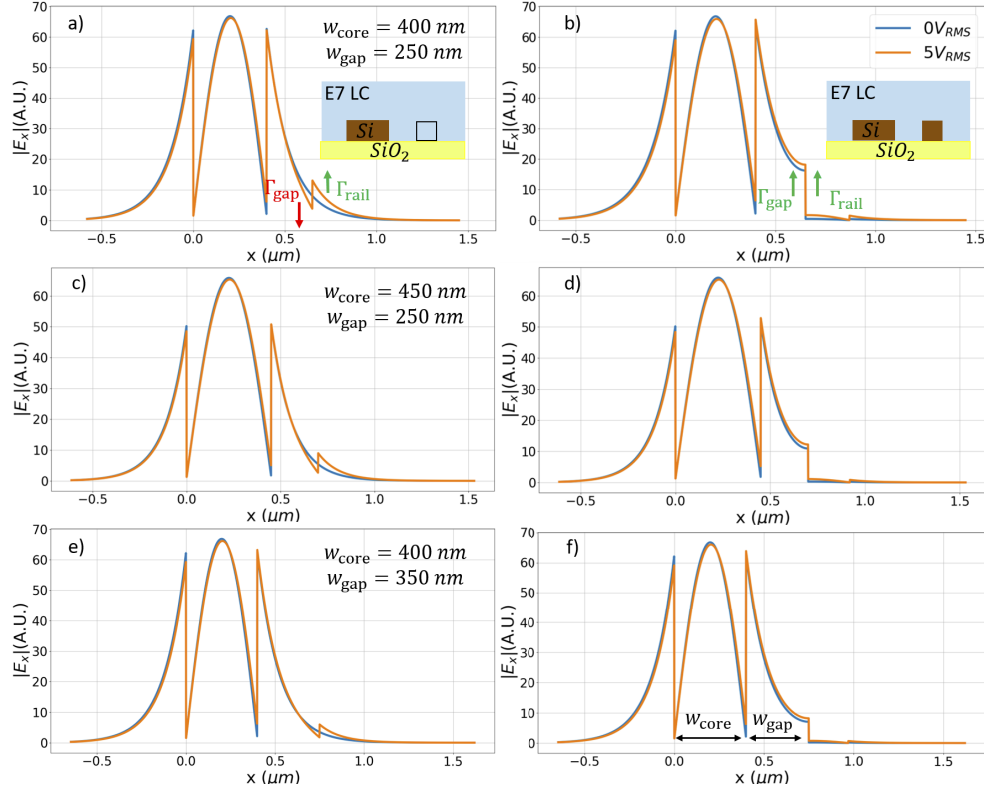

Fig. 4. The *x*-component of the electric field strength on the dashed line in Fig. 3. Simulation results are shown for the three measured devices in this work. Graphs a), c) and e) (the left column) show simulation results of a hypothetical side-rail filled with E7 LC oriented as in Fig. 1(a)) ($n = n_e$), graphs b), d) and f) (the right column) show simulation results with a silicon side-rail ($n = 3.45$).When $V = 0V_{RMS}$ the LC is oriented as in Fig. 1(a)), when $V = 5V_{RMS}$ the LC has an orientation as in Fig. 1(b)). The increase (decrease) of Γ_{gap} and Γ_{rail} between $V = 0\ V_{RMS}$ and $V = 5\ V_{RMS}$ is visualized in green (red).

The situation where the index of the E7 LC filled side-rail matches the surrounding LC cladding can be clearly identified on graphs a), c) and e) in Fig. 4 due to the continuous evanescent tail in the when $V = 0\ V_{RMS}$.

$$\Gamma_{core} = \frac{\iint_{core} |E_x|^2}{\iint_{total} |E_x|^2}$$

The calculated confinement factors Γ in Table 1 show that increasing the index of the side-rail decreases the confinement in the waveguide core Γ_{core} while boosting Γ_{gap}. This is the main contributor to the difference in electro-optic response between devices with a different w_{core}. The increase in evanescent field strength in devices with smaller core widths leads to a stronger response to changes in the waveguide cladding. The device with both smallest core width and
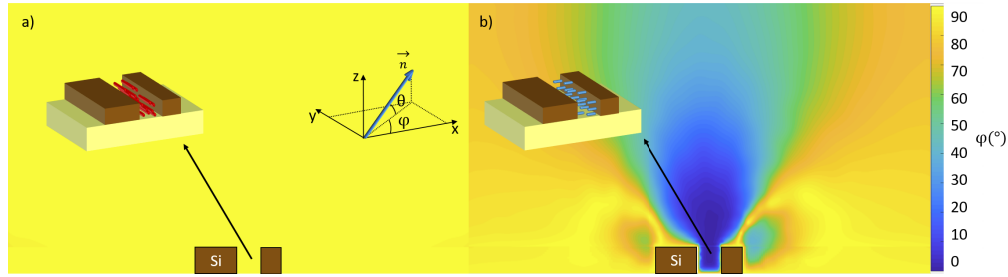
Fig. 5. Simulation of the twist of the director (in-plane rotation), with a) $0V_{RMS}$ actuation and b) $5\,V_{RMS}$ actuation. When a voltage above the threshold is applied, the director in the gap reorients towards the x-axis, but close to the waveguide interface surface interactions inhibit this rotation.

gap size has the strongest change in confinement induced by the side-rail. To get a more detailed picture of how the high index side-rail affects the distribution of $|E_x|^2$ in the cladding and how w_{gap} influences this, we calculated the fraction of $|E_x|^2$ in certain regions of the cladding in more detail for different geometries. These calculations are again performed with $V = 0\,V_{RMS}$, meaning the LC director in the gap is aligned with the waveguide as shown in Fig. 1(a).

$$\Gamma_{gap} = \frac{\iint_{gap} |E_x|^2}{\iint_{total} |E_x|^2}, \Gamma_{rail} = \frac{\iint_{rail} |E_x|^2}{\iint_{total} |E_x|^2}$$

Table 1 shows different values for Γ_{gap} and Γ_{rail} (%) of the geometry as shown in Fig. 3. Increasing the index of the side-rail increases Γ_{gap} (as was seen in the electric field strength plotted in Fig. 4) and lowers Γ_{rail}, similar to the increased electrical field strength in a slot waveguide mode. The device *wg400g250* has the largest Γ_{gap} and Γ_{rail}.

Table 1. Fraction (%) of $|E_x|^2$ in the areas colored on Fig. 3 for each device calculated with a side-rail filled with E7 LC oriented as in Fig. 1(a)) and a silicon side-rail.

device	wg400g250	wg450g250	wg400g350
Γ_{core} (brown area)			
E7 LC	60,07	68,06	60,02
Silicon	59,18	67,64	59,82
Γ_{gap} (red area)			
E7 LC	11,03	7,77	10,76
Silicon	12,00	8,28	10,98
Γ_{rail} (green area)			
E7 LC	0,101	0,052	0,017
Silicon	0,054	0,024	0,01

Table 1 confirms that the silicon side-rail increases the sensitivity to director changes in the gap, because of the increased field strength, as can be noticed by comparing the curves labeled $V = 0V_{RMS}$ on Fig. 4. Graphs a), c) and e) exhibit a continuous evanescent tail while graphs b), d) and f) have a discontinuity due to the silicon side-rail, leading to an increased field strength in the gap. Note that for this study we ignored the secondary E_y component parallel to the waveguide. We expect that its inclusion will slightly diminish the resulting phase shift, as the actuation of the liquid crystal rotates the director from an y alignment to an x alignment.

2.3. Electro-optic simulations

2.3.1. Modeling the liquid crystal

The response of the liquid crystal to voltages and geometry can be modeled using the finite element method, resulting in the spatial distribution of the director variation of the liquid crystal cladding. [17] An example result of the director variation from simulation is shown in Fig. 5. In Fig. 5(a)) no voltage is applied and the director is aligned with the *y*-direction ($\varphi = 90°, \theta = 0°$), the situation as given in Fig. 1(a)). In Fig. 5(b)) the applied voltage ($V = 5\,V_{RMS}$) aligns the director with the field lines, resulting in director rotation in the gap aligned to the *x*-axis, as shown in Fig. 1(b)). Close to the waveguide surface interactions inhibit the rotation. This director distribution corresponds to a spatially dependent refractive index in the cladding for the optical modes in the waveguide core. This data is fed into a fully anisotropic optical mode solver which can calculate Δn_{eff} of the propagating mode in the waveguide core in relation to the applied voltage.

From Δn_{eff}, the resulting phase shift with $L_{device} = 50\,\mu m$ can be calculated using Eq. (1) at $\lambda_0 = 1.55\,\mu m$. This results in the curves plotted in Fig. 6.
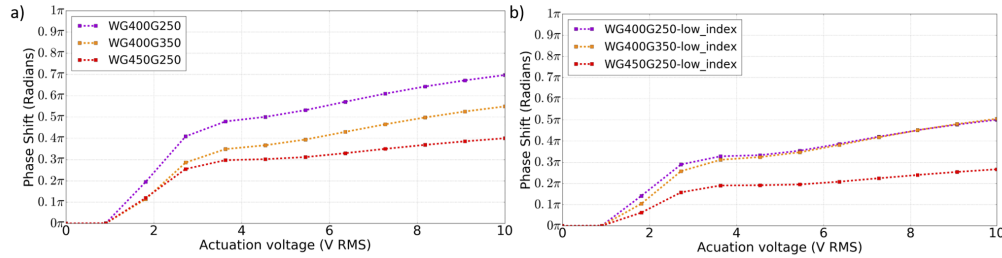

Fig. 6. a) Simulation ($\lambda_0 = 1550\,nm$) of devices with strong (infinite) molecular anchoring strength to the surface. Both w_{core} and w_{gap} influence the response. b) Simulation of devices with a side-rail filled with E7 LC (matching the anisotropy of the LC as shown in Fig. 1(a)).

Three important regimes can be observed from the simulation results shown in Fig. 6. Below $1\,V_{RMS}$ the LC director does not respond to applied voltages, but beyond a threshold voltage an S-shaped curve is obtained. This threshold is known as the Fréedericksz transition and is determined by the material parameters of the used LC (E7 mixture in these simulations and measurements). [18] Intuitively it can be understood as the minimum energy required for $\vec{E}_{actuation}$ to overcome elastic forces in the LC. For narrower gaps, the increase in anchoring strength and electric field (for a given voltage) roughly counteract each other, which results in a threshold voltage independent of w_{gap}:

$$V_{th} = \pi \sqrt{\frac{K}{\varepsilon_0 \Delta \varepsilon}}$$

with $\Delta \varepsilon$ the dielectric anisotropy and K the constant related to the elastic forces caused by the distortion of molecules due to $\vec{E}_{actuation}$.

After the threshold there is a strong increase associated with director change in the gap, which saturates between $4\,V_{RMS}$ and $5\,V_{RMS}$ followed by a much smaller secondary increase of the phase shift. In the saturation regime, where the director in the gap is fully reoriented (configuration as shown in Fig. 1(b)), a small linear change in phase still accumulates as a consequence of LC reorientation on the opposite side of the waveguide, where at $5\,V_{RMS}$ the director starts to respond to fringe fields, as can be seen in Fig. 5(b)).

These simulations indicate that the phase shift is in general larger for smaller w_{core} and w_{gap}, which is consistent with the confinement factors Γ_{gap} given earlier in Table 1. A smaller w_{core}

exhibits lower confinement, increasing the sensitivity to any changes in the cladding. A narrower w_{gap} leads to stronger actuation fields $\vec{E}_{actuation}$ for the same applied V_{RMS}, which in turn enhances the liquid crystal responsivity (slope).

The boundary conditions of the liquid crystal region determine the initial orientation of the director at 0 V_{RMS}. The boundary conditions at the physical boundaries of the LC domain, i.e. the surfaces of the waveguide, side-rail and buried oxide, determine the behaviour of the director in the neighbourhood of the surface. The director is anchored to the surface (the molecules are attracted to the surface, inhibiting reorientation close to the surface), meaning that a minimal energy $W_{anchoring}$ is required to dislodge the director from its anchored position on the surface. This anchoring energy determines the behaviour of the director close to the surfaces. In our simulations the anchoring conditions on the surfaces are set with the director as shown in Fig. 1(a), causing the LC to be aligned according to Fig. 5(a) when no $\vec{E}_{actuation}$ is present. [13]

Different anchoring conditions of the LC director can be applied in these electro-optic simulations. We applied a default of strong anchoring ($W_{anchoring} = \infty$) in our simulations. The weak anchoring ($W_{anchoring} = 10^{-4} J/m^2$) conditions increase the responsivity of the director to the applied voltage close to the surfaces. (This is also visualized in the director plots in Fig. 7(a),b). When we apply weak anchoring conditions the electro-optic response is enhanced, as is shown in Fig. 8. As the optical power increases inside the gap closer to the waveguide, the anchoring conditions are an important factor in these experiments. As real anchoring energies are unknown, the strong and weak anchoring simulations serve as boundaries for an expected range of values for the experimentally observed phase shifts. The decrease in phase shift on Fig. 8 can be explained because of the tilt θ of the director on the top surface of the waveguide caused by electric field lines outside of the gap (as can be noticed in Fig. 7). Because the weak anchoring causes the gap to saturate before the field lines outside the gap (fringe fields) manifest for this reorientation, this is visible in the electro-optic curve as a different regime, but only when weak anchoring is used in the simulation.
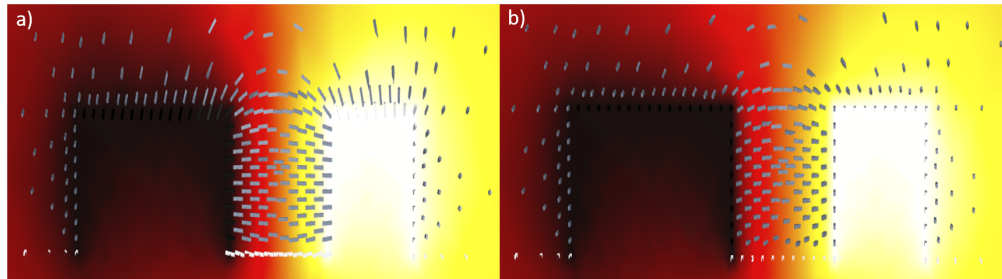

Fig. 7. LC director plot for a) weak anchoring and b) strong anchoring. The color gradient represents electric potential. In this simulation $V = 3\ V_{RMS}$

2.3.2.   Influence of side-rail index on the electro-optic response

We simulated the electro-optic response of each device for a silicon side-rail and the hypothetical case from section 2.2 where we have a side-rail with the same refractive index as E7 LC. Although the smaller w_{gap} increases the response of the LC director in the gap to the applied voltage in the low index case (as is predicted by theory due to an increased $\vec{E}_{actuation}$ for an equal RMS-voltage, and pushing the maximum of the director profile closer to the waveguide edge), a silicon side-rail will enhance the overlap with the optical mode in the gap, as can be seen in Fig. 6(a)) (and is predicted with Table 1).

Simulation results with an E7 LC filled side-rail (Fig. 6(b))) show that the devices with $w_{core} = 400\ nm$, $w_{gap} = 250\ nm$ (wg400g250) and $w_{core} = 400\ nm$, $w_{gap} = 350\ nm$ (wg400g350)
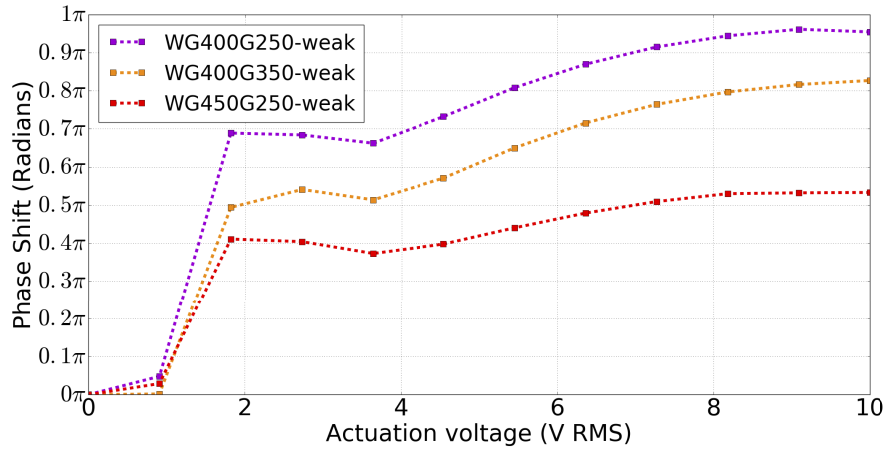
Fig. 8. Electro-optic response for liquid crystal with weak anchoring (weak attraction to surfaces).

have a different slope, but similar values in the saturation regime even though the narrower gap has a larger Γ_{gap}. This suggests that the increase of Γ_{gap} is not the only contribution to the increase of response with a high index side-rail, and the small but non-zero Γ_{rail} also is important for the increase electro-optic responses.

The change in distribution of the evanescent field can be tracked by assuming conservation of energy of the field component when actuating:

$$\Delta\Gamma_{rail} + \Delta\Gamma_{core} + \Delta\Gamma_{gap} + \Delta\Gamma_{clad} = 0$$

This means the confinement will always be lowered in other regions to facilitate an increase in regions of interest. Using a side-rail which is index matched to E7 LC, $\Delta\Gamma_{gap} + \Delta\Gamma_{clad} < 0$, which indicates the Δn_{eff} actually originates from the increasing confinement in the waveguide core (high index) and side-rail (low index), leading to a weaker net effect on Δn_{eff}. This is also visualized in Fig. 4 on graph a) (and can be noticed on graphs c) and e)), where one can notice the increase of Γ_{rail} accompanied by a decrease in Γ_{gap}. Because the hypothetical side-rail with E7 LC (oriented as Fig. 1(a)) is index matched, increasing Γ_{rail} has no effect on Δn_{eff}. The refractive index of the LC in the gap increases when $V = 5\ V_{RMS}$ (due to an interaction of $|E_x|$ with Δn_{eff}) but Γ_{gap} will be lowered at the same time.

When the same analysis is performed for a high-index silicon side-rail, the optical field redistribution is drastically different, because now $\Delta\Gamma_{core} + \Delta\Gamma_{clad} < 0$. In this case the increase of Γ_{rail} interacts with the high refractive index of silicon, just like the increasing Γ_{gap} interacts with an increasing refractive index, both contributing to a stronger Δn_{eff}. These changes can be observed in Fig. 4 in graphs b), d) and f), where one can notice an increase of both Γ_{gap} and Γ_{rail} when comparing the mode profiles for $V = 0\ V_{RMS}$ with the mode profiles when $V = 5\ V_{RMS}$ (as indicated on graph b)).

To investigate to which degree the silicon side-rail contributes more to Δn_{eff}, the changes in confinement are tracked when actuating the geometry with a silicon side-rail from $V = 0\ V_{RMS}$ to $V = 5\ V_{RMS}$, and results are listed in Table 2.

Table 2 shows that the $\Delta\Gamma_{rail}$ becomes smaller for larger gaps. This indicates that the higher refractive index of the side-rail adds an important contribution to Δn_{eff}. The numbers in Table 2 are in agreement with the simulated response curves Fig. 6(a),b, showing an increased influence of the silicon side-rail for smaller gaps.

Table 2. Fraction (%) of change in confinement in the areas colored on Fig. 4 for each device calculated with a silicon side-rail (n = 3.45).

device	*wg400g250*	*wg450g250*	*wg400g350*
$\dfrac{\Delta\Gamma_{\text{rail}}}{\lvert\Delta\Gamma_{\text{core}}+\Delta\Gamma_{\text{clad}}\rvert}$	11,52	11,82	8,41
$\dfrac{\Delta\Gamma_{\text{gap}}}{\lvert\Delta\Gamma_{\text{core}}+\Delta\Gamma_{\text{clad}}\rvert}$	88,48	88,18	91,59

This analysis shows that the side-rail does more than just provide an nearby electrode for the liquid crystal actuation. The use of a silicon side-rail draws the optical field into the gap area, making it more responsive to changes of the LC director in the gap compared to the use of a side-rail filled with E7 LC. The applied voltage then leads to a director rotation, which in turn will decrease the confinement factor of the waveguide core. This makes the optical mode interact more with the silicon side-rail, which becomes an important contributor to the effective index change of the optical mode when the gap gets narrower.

3. Fabrication

The fabrication of this phase shifter requires multiple steps. The underlying platform is IMEC's established iSiPP50G silicon photonics technology [2]. To bring liquid crystals in proximity with the waveguides, the back-end-of-line dielectric stack needs to be locally etched back, and the waveguides need to be exposed on three sides (top and sidewalls) without damaging the other parts of the silicon circuits, as can be seen in Fig. 9. Then the liquid crystal needs to be deposited.
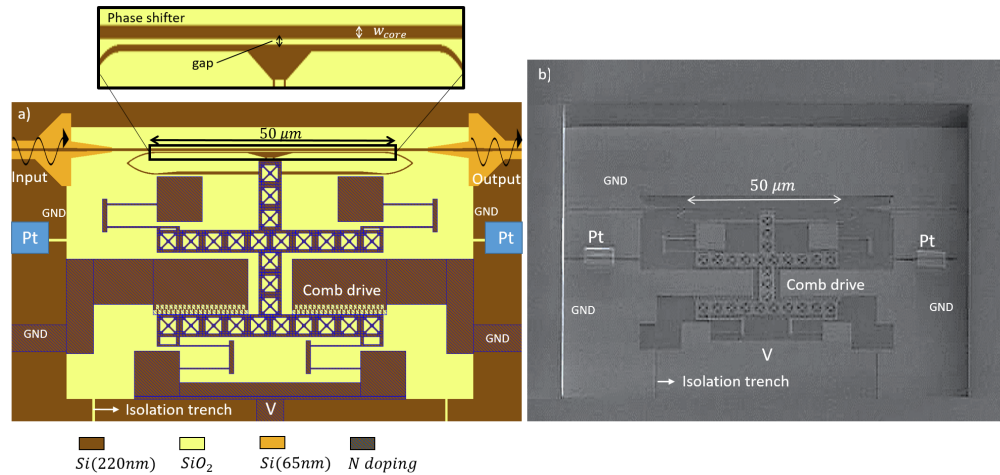

Fig. 9. a) Layout of the phase shifter. N-doped silicon is used as an electrical connection between the metal routing and the actual device. Two blue rectangles indicate the position where platinum was deposited to bridge an etched isolation trench on each side, connecting the optical waveguide electrically to the ground.

The devices on which we test this phase shifter concept were not originally designed for the use of liquid crystals, but for MEMS actuation [4]. Because of that, we need to perform also a small local post-processing step before depositing the liquid crystals, to electrically connect the side-rail with the external bond pads.

3.1.   *Exposing the silicon waveguide and side-rail structures*

Because the iSiPP50G platform incorporates modulators, photo-detectors and two layers of Cu interconnects, the back-end-of-line dielectric stack needs to be locally etched back to expose the waveguides, as can be seen in Fig. 9. This process step is also used for other applications where access to the waveguides is needed, such as sensors. This creates a local recess of 5-6 µm around each device. After this initial opening, which exposes the top of the waveguides, we applied a short timed etch with buffered hydrofluoric acid (HF) etch to clear the sidewalls of the waveguides and the narrow trench between the waveguide and the narrow silicon rail on the side. There is no significant undercut into the buried oxide underneath the waveguides.

Even though the phase shifter device was originally conceived to be used as a MEMS actuator [4], we do not perform the final fabrication steps where the oxide underneath the waveguide is selectively removed [19]. The cross section of the optical part of the device is therefore similar to the desired cross section shown in Fig. 1. This allows us to use these MEMS-devices as a proof-of-concept demonstrator for a liquid crystal phase shifter, and confirming the integration potential with IMEC's iSiPP50G silicon photonics platform without perturbing the integrated active devices such as modulators and germanium photodetectors.

In Fig. 9, the MEMS phase shifter design used in these experiments is shown [4]. For the liquid crystal actuation, the waveguide needs to be electrically connected to ground, so two additional strips of Pt were added using ion-beam induced deposition (IBID), in order to bridge the electrical insulation trenches of the originally intended MEMS operation and electrically connect the rail to the N-doped silicon used as electrical routing to the standard iSiPP50G metal wiring and standard bond pads.

3.2.   *Liquid crystal deposition*

The initial demonstration of this phase shifter principle was carried out using a manual fiber dip deposition [20] to fill the recessed cavity around the phase shifter with liquid crystal. The subsequent experiments presented in this work use an inkjet printing technique for precise local deposition of the liquid crystal instead of the fiber dip deposition. Multiple open recessed cavities can be automatically filled with the correct volume of liquid crystal. The principle and the results of this deposition technique are shown in Fig. 10, where an E7 liquid crystal mixture has been successfully deposited in the cavities. [21,22]
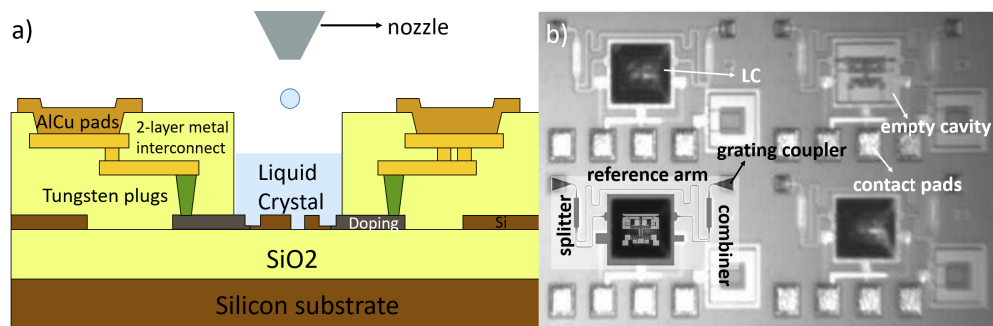

Fig. 10. Deposition a) Schematic of the inkjet printer deposition. The LC can be deposited locally in an open cavity. b) Optical microscope image of four cavities, of which three are filled. Black annotations show the circuit elements of the unbalanced Mach-Zehnder interferometer.

The key advantage of moving to an inkjet printing approach is that the deposition can be controlled and localized, making the process reproducible and scalable, and avoiding interference with other optical components such as grating couplers and regular waveguides. In earlier

demonstrations of silicon photonic devices with liquid crystals, the liquid crystal was always covering large areas, or even the entire chip surface. [7,12], making it impractical for widespread application.

4. Measurements and discussion

4.1. Measurement

The transmission spectra of all devices were measured by sweeping the amplitude of an applied square wave with frequency of 1 kHz. This modulation is commonly used for liquid crystal cells to reduce charge accumulation due to ion drift. The LC director aligns to the field lines but not to the sign of the direction because there is no permanent dipole moment across the entire molecular axis. [23,24] This electric field alignment occurs due to the dielectric anisotropy $\Delta\varepsilon$, leading to a stronger polarizability on the long axis of the molecules. The results are shown in Fig. 11.

To measure the induced phase shift from an amplitude transmission measurement, the three devices with varying core width or gap are each embedded in an on-chip unbalanced Mach-Zehnder interferometer (MZI) circuit using a 50/50 MMI (MultiMode Interferometer) splitter and combiner (illustrated on Fig. 10). From the wavelength shift in the transmission spectra we then extract the phase shifts as a function of the amplitude of the applied square wave.

The 0 V measurements were omitted from these plots as they turned out to be difficult to reproduce: they exhibited unexpected shifts and noisy patterns, indicating instabilities in the LC director configuration when no voltage is applied. Our hypothesis is that, because there is only a well defined alignment close to edges (as explained in section 2.3.1), but no other alignment is defined (i.e. covering glass with rubbing layer), the LC further away from edges experiences conflicting alignment conditions. Interaction with the etched structures of the unused comb-drive can perturb the desired alignment as defined in Fig. 1(a)), and conflicting alignment conditions might create instability and cause a time varying index in the cladding on top of the waveguide. Such unpredictable behaviour on top of the waveguide also results in arbitrary phase shifts. Earlier work [7] indicated that there might be a lower threshold voltage for tilting molecules on top of the waveguide, which could explain the instability below the threshold of the gap. Future studies will have to determine the actual cause. As the LC is also exposed to the air, particles and sound waves can also interact with the cladding leading to undesirable perturbations. The undefined surface properties (untreated surfaces before deposition of the LC) could have an influence as well.

It was also observed that the phase tuning effect has a threshold of at least 2 V, a somewhat higher than expected from the value of the Fréedericksz threshold of the LC $\vec{E}_{\text{actuation}}$. [18] This is why in this work, we use the more reproducible 1 V_{RMS} measurement as the reference for the measured phase shift at higher voltages. We did not observe a shift or drift of the spectra beyond the noise over time. A measurement of a device several days later yielded similar spectra (both the reference at 1 V_{RMS} and the spectra at higher voltages) with no drift of the reference or changes in obtained phase shift and extracted electro-optic curve.

The transmission spectra in Fig. 11 show a great deal of noise. This can be attributed to phase flicker in the liquid crystal during the modulation, and this noise in the time domain translates into a noise on the transmission spectrum as the wavelength is swept. The phase flicker can be reduced by increasing the frequency of the quasi-static actuation field $\vec{E}_{\text{actuation}}$ (see Supplement 1), but in the implementation presented here the speed of the drive signal is limited by the electrical characteristics (resistance (R) and capacitance (C)) of the MEMS designs with deposited Pt bridges we used for this experiments. The comb-drive and the waveguide become parallel capacitors, increasing the capacitance and thus the RC time constant ($\tau = RC$). As can be seen on Fig. 9(a)), the N-doping serving as electrical routing does not go up to the Pt bridges, increasing the resistance and the time constant as a consequence. The quality of the Pt bridges
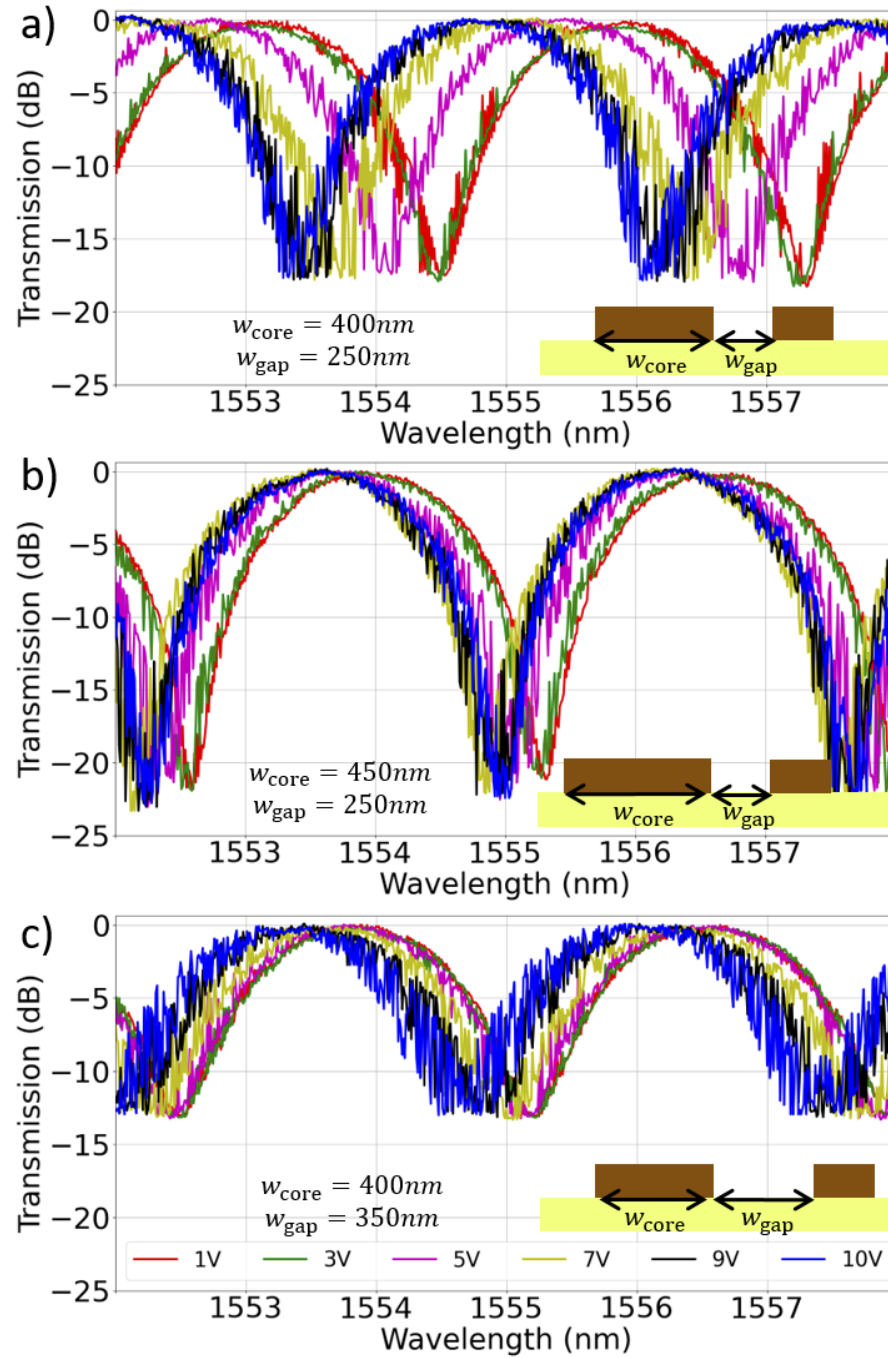
Fig. 11. Three normalized transmission spectra of different phase shifter devices in an unbalanced MZI. Each device has either a different waveguide core width or gap size. a) $w_{core} = 400nm, w_{gap} = 250nm$. b) $w_{core} = 450nm, w_{gap} = 250nm$. c) $w_{core} = 400nm, w_{gap} = 350nm$. Colors indicate the amplitude of the applied square wave. The 'noise' on the transmission spectra is a sign of phase flicker in the LC.

cannot be assessed and they might also have a high resistance, and could induce a capacitance in series to the actual device capacitance potentially causing a voltage drop.

The parasitic director changes in the "bulk" of the liquid crystal can be seen in Visualization 1, where the interplay of ambient visible lighting and the LC surface shows a somewhat chaotic behaviour of the director in the bulk.

The extinction ratio of the transmission curve remains constant during actuation, indicating little or no change in optical losses in the phase shifter. Any change in absorption or scattering losses in the phase shifter would affect the balance in the MZI (in either positive or negative direction) which can be observed in the extinction ratio. We could not observe such a change within the precision allowed by the phase-flicker noise on the transmission spectra.

Figure 12 shows the extracted phase shift, obtained from fitting a sine function to the MZI transmission spectra on a linear scale. The phase of the fitted sine corresponds to the phase shift induced by the LC phase shifter.
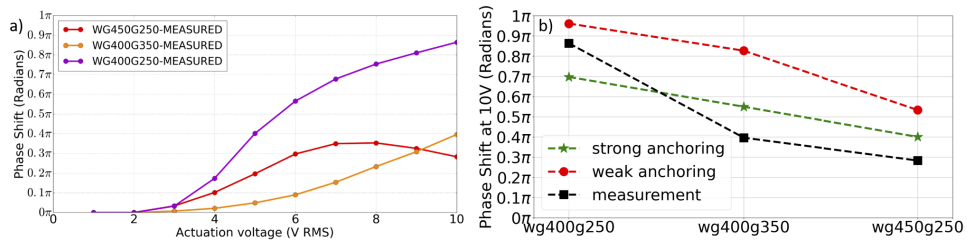

Fig. 12. a) Extracted phase shift from fitting sinusoidal function on transmission spectrum b) extracted phase shift at $V = 10 \, V_{\mathrm{RMS}}$ from measurement compared to simulations with weak and strong anchoring

All devices exhibit a similar threshold voltage, but each shows a distinct response. As expected, it appears that a wider gap leads to a lower responsivity (slope), but changing the waveguide core size has a more pronounced influence on the saturation value (as discussed earlier this has the strongest influence on the confinement factor of the waveguide). The responses exhibit a higher threshold voltage as reported in earlier measurements [25], and this is a strong indication of a voltage drop elsewhere in the device. This can be attributed to the fact that the device was not designed for this purpose and we had to modify it with an additional Pt deposition step, and it is impossible to assess the quality of the bridged trenches with the Pt deposition. Also, the comb drive structure of the MEMS design can introduce unknown electrical effects as well as disrupt the director orientation in the liquid crystal.

4.2. Comparing measurements to electro-optic simulations

The simulated phase shifts at $V = 10 \, V_{\mathrm{RMS}}$ (limit of the measurement setup) of the different anchoring conditions are shown in Fig. 12(b) together with the measured phase shifts, where the comparison between devices in simulation (weak and strong anchoring serve as upper and lower boundary of expected values) and the measurements are in better agreement. In reality, it is possible that each individual device is subjected to different surface conditions leading to different anchoring energies, as there could be fabrication variations in the geometry (the etch depth could vary, which is expected to have a strong influence) or undefined surface properties, because there was no additional surface treatment before depositing the E7 LC with inkjet printing.

A change in geometry can not only influence the anchoring conditions but also influence modal confinement in the waveguide core. Changes in gap size will result in different values of $\vec{E}_{\mathrm{actuation}}$ for similar voltages, resulting in different reorientation of the LC director for different devices at the same RMS-voltage.

The required length for a π phase shift for $V = 10\ V_{\mathrm{RMS}}$ is calculated. Results are shown in Table 3. To extract the $V_\pi L_\pi$ product from the measurements, we look for the maximum slope in the response curves, which are obtained using the 1V spectrum of each device as reference. On such an operating point the sensitivity to a change in voltage is maximal, so a small signal applied to this bias point has a maximum effect. For devices with $w_{\mathrm{gap}} = 250\ nm$ this point is situated around 5 V. The device with $w_{\mathrm{gap}} = 350\ nm$ has no observed maximum slope inside the measurement range, the maximum slope is found to be at 10 V (but could be located at a higher voltage). The significant influence of gap to this optimal bias is an indication of another capacitor in series in the network. A wider gap means a smaller capacitance, which increases the voltage drop caused by a series capacitance.

Table 3. Required length for π phase shift at 10 V, calculated $V_\pi L_\pi$ (*V.mm*) for small signal modulation at maximum slope of response and extract losses from MZI power imbalance.

device	wg400g250	wg450g250	wg400g350
L_π (10V) (*μm*)	57,88	176,72	126,25
$V_\pi L_\pi$ (*V.mm*)	0,2198	0,4987	0,5710
α (*dB*)	1,53	0,833	2,257

The loss of each device was estimated using the extracted MZI power imbalance (ratio between power in arms) from the extinction ratio. This means the insertion loss and power imbalance from the MMIs is included in the reported loss, as is the case for the transitions to the etched recess. Earlier work with infiltrated slot waveguides in [25] exhibited an estimated loss of $10 \pm 1\ dB$ which consists of the lumped loss of two strip-slot waveguide transitions and the propagation loss of a 1 mm slot waveguide. Even though the propagation loss of slot waveguides can be as low as 6.5 ± 0.2 dB/cm [26], the high losses in these measurements are suspected to originate from the unavoidable strip-slot waveguide transitions. Therefore we expect the loss in our devices to be considerably reduced, because we maintain a simple strip waveguide geometry, without need for difficult tapering between very distinct mode profiles. But on the other hand, our best performing device has a voltage × length product $V_\pi L_\pi$ that is about 10× higher, i.e. a 10× lower efficiency. However, for scalable circuits with a large number of tunable devices, insertion loss is the more critical performance metric, and this is a strong point of the side-rail approach compared to the slot waveguide, as we can avoid the loss of the strip-slot transitions. We plan to elaborate and optimize the insertion loss and back-reflection of this architecture with future experiments using dedicated designs.

When we compare this work to [11] there is a major reduction of the operational voltage (in [11] $V_{\max} = 120\ V_{\mathrm{RMS}}$). We have an improved $V_\pi L_\pi$ (in [11] $V_\pi L_\pi = 0.72\ V.cm$) and comparable total insertion loss.

5. Conclusions

We demonstrated a proof-of-concept of a silicon photonics phase shifter based on liquid crystal actuation, directly integrated in IMEC's full silicon photonics platform. The open recessed cavities in IMECS's platform enable localized exposure of waveguide structures and inkjet printing delivers precise localized liquid crystal deposition, allowing side-by-side operation of the liquid crystal with other active and passive optical components in the platform.

The phase shifter uses a lateral silicon electrode to induce a strong $\vec{E}_{\mathrm{actuation}}$ with a relatively low voltage on the side of the waveguide. This enables liquid crystal reorientation below 5 V_{RMS}. This device has lower insertion loss compared to previously demonstrated slot waveguide systems, but with a lower efficiency. While this proof of concept demonstrates the viability of this actuation mechanism, there are still many opportunities for improvements. First of all, this design was

originally not intended for this form of actuation, and the additional design features for MEMS actuation (e.g. the comb drive) can strongly perturb the arrangement of the liquid crystal. Also, we only used actuation on a single side, but simulations indicate that a two-sided electrode could achieve 2π phase shift within a length of 50 μm. Also, the geometry of the electrical connections can be further be optimized, and the measurements presented here show signs of phase flicker. Addressing these shortcomings is the subject of follow-up experiments with designs specifically aimed to demonstrate liquid crystals as a viable tuning option for large-scale silicon photonic circuits.

Disclosures. The authors declare no conflicts of interest.

Data Availability. Measurement data available in Dataset 1 [27].

Supplemental document. See Supplement 1 for supporting content.

References

1. P. P. Absil, P. Verheyen, P. D. Heyn, M. Pantouvaki, G. Lepage, J. D. Coster, and J. V. Campenhout, "Silicon photonics integrated circuits: a manufacturing platform for high density, low power optical I/O's," Opt. Express **23**(7), 9369–9378 (2015).
2. M. Pantouvaki, S. A. Srinivasan, Y. Ban, P. De Heyn, P. Verheyen, G. Lepage, H. Chen, J. De Coster, N. Golshani, S. Balakrishnan, P. Absil, and J. Van Campenhout, "Active Components for 50 Gb/s NRZ-OOK Optical Interconnects in a Silicon Photonics Platform," J. Lightwave Technol. **35**(4), 631–638 (2017).
3. A. Masood, M. Pantouvaki, G. Lepage, P. Verheyen, J. V. Campenhout, P. Absil, D. V. Thourhout, and W. Bogaerts, "Comparison of heater architectures for thermal control of silicon photonic circuits," in *Proceedings of the 10th International Conference on Group IV Photonics*, (2013), p. ThC2.
4. P. Edinger, A. Y. Takabayashi, C. Errando-Herranz, U. Khan, H. Sattari, P. Verheyen, W. Bogaerts, N. Quack, and K. B. Gylfason, "Silicon photonic microelectromechanical phase shifters for scalable programmable photonics," Opt. Lett. **46**(22), 5671–5674 (2021).
5. T. Wei, P. Chen, M.-J. Tang, G.-X. Wu, Z.-X. Chen, Z.-X. Shen, S.-J. Ge, F. Xu, W. Hu, and Y.-Q. Lu, "Liquid-crystal-mediated active waveguides toward programmable integrated optics," Adv. Opt. Mater. **8**(10), 1902033 (2020).
6. B. Berteloot, I. Nys, X. Xue, J. Beeckman, and K. Neyts, "Rotationally invariant ring-shaped liquid crystal structures between two substrates with different photoalignment," J. Mol. Liq. **337**, 116238 (2021).
7. W. De Cort, J. Beeckman, T. Claes, K. Neyts, and R. Baets, "Wide tuning of silicon-on-insulator ring resonators with a liquid crystal cladding," Opt. Lett. **36**(19), 3876–3878 (2011).
8. C.-T. Wang, Y.-C. Li, J.-H. Yu, C. Y. Wang, C.-W. Tseng, H.-C. Jau, Y.-J. Chen, and T.-H. Lin, "Electrically tunable high q-factor micro-ring resonator based on blue phase liquid crystal cladding," Opt. Express **22**(15), 17776–17781 (2014).
9. T. Ako, A. Hope, T. Nguyen, A. Mitchell, W. Bogaerts, K. Neyts, and J. Beeckman, "Electrically tuneable lateral leakage loss in liquid crystal clad shallow-etched silicon waveguides," Opt. Express **23**(3), 2846–2856 (2015).
10. Y. Atsumi, K. Watabe, N. Uda, N. Miura, and Y. Sakakibara, "Initial alignment control technique using on-chip groove arrays for liquid crystal hybrid silicon optical phase shifters," Opt. Express **27**(6), 8756–8767 (2019).
11. K. J. Sundar, A. Marinins, B. Figeys, R. Jansen, X. Rottenberg, P. Kula, J. Beeckman, M. S. Dahlem, and P. Soussan, "Liquid crystal based active phase modulator for silicon nitride photonics circuits at near-infrared," *Conference on Lasers and Electro-Optics* p. SF2O.5 (2020).
12. Y. Xing, T. Ako, J. P. George, D. Korn, H. Yu, P. Verheyen, M. Pantouvaki, G. Lepage, P. Absil, A. Ruocco, C. Koos, J. Leuthold, K. Neyts, J. Beeckman, and W. Bogaerts, "Digitally Controlled Phase Shifter Using an SOI Slot Waveguide With Liquid Crystal Infiltration," IEEE Photonics Technol. Lett. **27**(12), 1269–1272 (2015).
13. H. Desmet, K. Neyts, and R. Baets, "Modeling nematic liquid crystals in the neighborhood of edges," J. Appl. Phys. **98**(12), 123517 (2005).
14. B. P. Singh, S. Sikarwar, K. K. Pandey, R. Manohar, M. Depriester, and D. P. Singh, "Carbon nanotubes blended nematic liquid crystal for display and electro-optical applications," Electronic Mater. **2**(4), 466–481 (2021).
15. A. Zheng, X. Chu, P. Wang, P. Wang, S. Gao, J. Yang, H. Lu, G. Deng, and Z. Yin, "The characterization and application of two liquid crystal mixtures in the low thz region," Crystals **10**(2), 99 (2020).
16. L. A. Al-Qurainy and K. A. A. Naimee, "Temperature effects on liquid crystal nonlinearity," in Liquid Crystals, P. K. Choudhury, ed. (IntechOpen, Rijeka, 2018), chap. 8.
17. J. Beeckman, R. James, F. A. Fernandez, W. De Cort, P. J. M. Vanbrabant, and K. Neyts, "Calculation of Fully Anisotropic Liquid Crystal Waveguide Modes," J. Lightwave Technol. **27**(17), 3812–3819 (2009).

18. R. E. Michel and G. W. Smith, "Dependence of birefringence threshold voltage on dielectric anisotropy in a nematic liquid crystal," J. Appl. Phys. **45**(8), 3234–3236 (1974).

19. W. Bogaerts, H. Sattari, P. Edinger, Y. A. Takabayashi, I. Zand, X. Wang, A. Ribeiro, M. Jezzini, C. Errando-Herranz, G. Talli, K. Saurav, M. Garcia Porcel, P. Verheyen, B. Abasahl, F. Niklaus, N. Quack, K. B. Gylfason, P. O'Brien, and U. Khan, "MORPHIC : Programmable photonic circuits enabled by silicon photonic MEMS," Proc. SPIE **11285**, 1 (2020).

20. L. Van Iseghem, U. Khan, P. Edinger, C. Errando-Herranz, A. Y. Takabayashi, H. Sattari, K. B. Gylfason, N. Quack, J. Beeckman, and W. Bogaerts, "Liquid crystal phase shifter integrated in a silicon photonics platform," in *European Conference on Integrated Optics (ECIO)*, (2020), pp. 1–3.

21. M. Moirangthem, A. F. Scheers, and A. P. H. J. Schenning, "A full color photonic polymer, rewritable with a liquid crystal ink," Chem. Commun. **54**(35), 4425–4428 (2018).

22. E. Parry, S. Bolis, S. J. Elston, A. A. Castrejon-Pita, and S. M. Morris, "Drop-on-demand inkjet printing of thermally tunable liquid crystal microlenses," Adv. Eng. Mater. **20**(3), 1700774 (2018).

23. P. Selvaraj, K. Subramani, B. Srinivasan, C.-J. Hsu, and C.-Y. Huang, "Electro-optical effects of organic n-benzyl-2-methyl-4-nitroaniline dispersion in nematic liquid crystals," Sci. Rep. **10**(1), 14273 (2020).

24. W. Gwizdala and Z. Gburski, "Molecular order and dynamics of 5cb liquid crystals in confined space - computer simulation," TASK Quarterly. Scientific Bulletin of Academic Computer Centre in Gdansk **19**, 35–64 (2015).

25. Y. Xing, T. Ako, J. P. George, D. Korn, H. Yu, P. Verheyen, M. Pantouvaki, G. Lepage, P. Absil, C. Koos, J. Leuthold, J. Beeckman, and W. Bogaerts, "Direct digital control of an efficient silicon+liquid crystal phase shifter," in Group IV Photonics 2014, (2014), pp. 43–44.

26. R. Ding, T. Baehr-Jones, W.-J. Kim, X. Xiong, R. Bojko, J.-M. Fedeli, M. Fournier, and M. Hochberg, "Low-loss strip-loaded slot waveguides in silicon-on-insulator," Opt. Express **18**(24), 25061–25067 (2010).

27. L. Van Iseghem, U. Khan, J. Beeckman, and W. Bogaerts, "Dataset 1 for low power optical phase shifter using liquid crystal actuation on silicon photonics platform," figshare (2021). https://doi.org/10.6084/m9.figshare.19653333